

Atomic transitions for adaptive optics

RUI YANG^{1,2}, JOSCHUA HELLEMEIER², AND PAUL HICKSON^{2,3,*}

¹*School of Physics and Astronomy, Yunnan University, South Section, East Outer Ring Road, Chenggong District, Kunming, 650500, China*

²*Department of Physics and Astronomy, University of British Columbia, 6224 Agriculture Road, Vancouver BC, V6T 1Z1, Canada*

³*National Astronomical Observatories, Chinese Academy of Sciences, A20 Datun Road, Chaoyang District, Beijing, China*

* *Corresponding author: hickson@physics.ubc.ca*

Compiled July 12, 2021

Adaptive optics systems using sodium laser guide stars are widely employed at major astronomical observatories. It is natural to ask whether other atomic species might offer advantages. In this paper we review all abundant atoms and ions in the upper atmosphere, including Na, Fe, Mg⁺, Si⁺, Ca⁺, K and also the non-metallic species N, N⁺, O, H, considering their potential for adaptive optics. Return fluxes for all transitions that can be excited using either one or two wavelengths were computed. We also considered multi-wavelength emission, comparing the performance of different transitions for polychromatic laser guide star (PLGS) adaptive optics. We find that of all the mesospheric metals, Na is the most suitable for both monochromatic and polychromatic laser guide stars, providing about six times more return flux than the best transitions in Fe. For high-altitude observatories, excitation at 330 nm in Na should give the highest PLGS performance. Atomic O, N and N⁺ have strong transitions and very high abundances in the mesosphere. This makes them potential candidates for the generation of intense laser guide stars by amplified spontaneous emission, if a suitable excitation process can be demonstrated. Direct excitation by CW lasers is impractical as all transitions from the ground state are beyond the atmospheric cutoff. Nevertheless, it may be possible using high-power pulsed lasers. © 2021 Optical Society of America

<http://dx.doi.org/10.1364/ao.XX.XXXXXX>

1. INTRODUCTION

Adaptive optics (AO) systems are employed by many ground-based telescopes to compensate atmospheric turbulence, thereby greatly improving the resolution of astronomical images [1]. Many of these systems employ laser guide star (LGS) beacons, which allow sensing of atmospheric turbulence in any desired direction, increasing sky coverage [2]. Large telescopes typically employ resonant LGS systems in which transitions in mesospheric atom are excited, typically the D_2 transition of neutral atomic sodium. Although other chemical species have been considered [3, 4], sodium is preferred due to its relatively-high abundance and strong resonance lines.

Despite the impressive success of AO systems employing sodium LGS, there are several reasons to reconsider other atoms and ions. The performance of such AO systems is limited by the return flux of the LGS, due to photon shot noise. Advances have been made both in increasing laser power, and improving the efficiency of sodium LGS [5–9]. For example, simulations indicate that repumping atoms from the D_{2b} ground state, in combination with circular polarization, can increase the return flux by a factor of 3 – 4 [6]. Nevertheless, any technique that might further increase the return flux would be valuable.

Several new techniques that might potentially achieve high-intensity LGS are discussed in [10]. One possible approach

is amplified spontaneous emission (ASE) [11]. In this idea, laser pumping of an abundant atmospheric atomic or molecular species could produce a population inversion that would amplify radiation generated by spontaneous emission. A critical requirement for ASE is a suitable transition for which the optical depth τ , defined as the integral of the absorption coefficient along the propagation path, is negative and has an absolute value that exceeds unity. This is a consequence of the equation of radiative transfer, from which it follows that the gain in intensity is proportional to $\exp(-\tau)$.

Another motivation for considering alternatives to sodium is the problem of atmospheric tilt indeterminacy [12]. Backscattered photons follow the same path as the transmitted beam, so the apparent position of the LGS is independent of wavefront tilt induced by the atmosphere. A number of techniques have been proposed to break this degeneracy (see, for example, [13, 14] and references therein). A promising approach is that of polychromatic laser guide stars (PLGS) [15, 16]. In this technique, a laser is used to generate emission at two or more widely-separated wavelengths. Because of differential refraction, the backscattered light propagates along different paths through the atmosphere. Thus one need not rely on natural guide stars to sense the atmospheric tilt. The differential positions of the PLGS at different wavelengths is small and must be measured

with high precision. Creating sufficiently-intense polychromatic emission is a challenge.

There is also a related problem of focus indeterminacy, as the sodium centroid altitude varies on short timescales [17]. This makes it difficult to separate atmospheric focus variations from other focus errors. This problem primarily affects very-large telescopes as the wavefront error due to focus variations increases in proportion to the square of the telescope aperture diameter [18].

The present paper examines atoms and ions in the upper atmosphere that might be useful for AO. We consider the abundance and distribution of all relevant species and compute the relative return flux for transitions that can be excited by ground-based lasers. Our aim is to identify potential transitions for monochromatic and PLGS, and to assess the feasibility of ASE.

2. MESOSPHERIC ATOMS AND PARAMETERS OF INTEREST

Meteoric ablation is the primary source of metallic species in the mesosphere and lower thermosphere (MLT) region of the atmosphere, at altitudes between 80 and 120 km. In this altitude range, the atmospheric density decreases from 10^{-5} to 10^{-8} kg m $^{-3}$ and collision rates are in the range $10^3 - 10^5$ s $^{-1}$. This is also the coldest region of the atmosphere. At mid-latitude sites, the temperature at the mesopause ranges from 178 – 192 K, at an altitude of 85 – 102 km, depending on the season [19].

Typical values of the column density N , altitude of the centroid of the density distribution, and the RMS width (vertical extent) for each species are listed in Table 1. For sodium, we use recent data by Gardner [20] to update earlier values listed by Happer [3]. The centroid altitude and RMS width for non-metallic species were computed from the MSIS-90 atmospheric model [21]. These were evaluated at midnight, January 1 for latitude $+30^\circ$ and longitude 0° .

The major meteoric species are Na, Fe, Mg and Si. There are also two less-abundant species, Ca and K. These metals exist as layers of atoms between about 80 and 105 km and occur primarily as atomic ions at higher altitudes. Below 85 km they form compounds: oxides, hydroxides, and carbonates, which polymerize into nanometer-sized meteoric smoke particles. Above 85 km, photolysis of N $_2$, O $_2$ and H $_2$ O by extreme ultraviolet (EUV) radiation leads to high concentrations of nitrogen, oxygen and hydrogen atoms. These atoms attack metallic compounds such as hydroxides and oxides, reducing them and thereby returning the metals to their atomic phase.

In a typical AO application, a laser is used to excite atoms from the ground state to an excited state. The atom then returns to the ground state via spontaneous and stimulated emission. Only spontaneous emission contributes to backscattered radiation since stimulated emission propagates in the same direction as the laser radiation. The LGS return flux can be computed from the equation of radiative transfer. For an optically-thin medium (optical depth $\tau \ll 1$) the specific intensity I_ν (W m $^{-2}$ Hz $^{-1}$ sr $^{-1}$) of the backscattered radiation is given by [10]

$$I_\nu(\nu) = \frac{h\nu}{4\pi} N A_{21} x \varphi(\nu) = \frac{2h\nu}{\lambda^2} N \sigma_{21}(\nu) x. \quad (1)$$

Here λ is the wavelength, $\nu = c/\lambda$ is the frequency, c is the speed of light in vacuum and N is the column density of atoms of this species. A_{21} is the Einstein A coefficient for the transition and the function $\varphi(\nu)$ is the mean line profile, normalized

Table 1. Parameters of mesospheric atoms and ions

Species	N m $^{-2}$	Altitude km	RMS width km	Sources
Na	4.0×10^{13}	91.5	4.6	[20]
Fe	10.2×10^{13}	88.3	4.5	[20]
Mg	1×10^{13}	89.4	4.2	[22, 23]
Mg $^+$	8×10^{13}	94.6	7.0	[22, 23]
Si $^+$	4×10^{13}	111.0	10.1	[24]
Ca	3.4×10^{11}	90.5	3.5	[20]
Ca $^+$	7.2×10^{11}	95.0	3.6	[20]
K	4.5×10^{11}	91.0	4.7	[20]
N	1×10^{18}	223.0	60.2	[21, 25]
N $^+$	1×10^{18}	-	-	[25]
O	6.5×10^{21}	110.3	28.7	[21, 26]
H	2.3×10^{18}	95.6	38.9	[21, 27]

so that its integral over frequency ν is unity. The dimensionless parameter x is the occupation fraction of the upper state, i.e. the equilibrium fraction of atoms found in this state under continuous excitation by a laser having specific energy density ρ_ν , and $\sigma_{21}(\nu)$ is the cross section for stimulated emission. The second equality follows from the relation between stimulated and spontaneous emission, $B_{21} = \lambda^3 A_{21} / 8\pi h$, and the definition

$$\sigma_{21}(\nu) \equiv \frac{h\nu}{c} B_{21} \varphi_\nu(\nu) = \frac{\lambda^2}{8\pi} A_{21} \varphi(\nu). \quad (2)$$

Here the subscript 1 denotes the lower (ground) state, 2 denotes the upper state, and B_{21} is the Einstein B coefficient for stimulated emission.

For a CW laser having beam area \mathcal{A} in the MLT, the return flux Φ , in units of photons s $^{-1}$ m $^{-2}$ is related to the intensity by

$$\Phi = \frac{\mathcal{A}}{z^2} \int_0^\infty \frac{I_\nu(\nu)}{h\nu} d\nu, \quad (3)$$

where z is the line-of-sight distance to the LGS.

In the mesosphere, Doppler broadening is the dominant line-broadening process. As the temperature varies within the MLT, the line profile is more precisely written as

$$\varphi(\nu) = \frac{1}{N} \int_0^\infty n(z) \varphi(\nu, z) dz, \quad (4)$$

where $n(z)$ is the number density of the atomic species under consideration at distance z along the line of sight. In practice, the function $\varphi(\nu)$ is well-represented by a Gaussian

$$\varphi(\nu) = \frac{2}{w} \sqrt{\frac{\ln 2}{\pi}} e^{-4 \ln 2 (\nu - \nu_0)^2 / w^2}, \quad (5)$$

where w is the line width at half maximum intensity. It depends on the characteristic temperature T in the MLT and the mass m of the atomic species,

$$w = \frac{1}{\lambda_0} \left(\frac{8k_B T \ln 2}{m} \right)^{1/2} \quad (6)$$

where k_B is Boltzmann's constant. Adopting $T = 180$ K results in a width for the sodium D line of 1.02 GHz.

The absorption cross section $\sigma_{12}(v)$ is given by

$$\sigma_{12}(v) = \frac{g_2}{g_1} \sigma_{21}(v), \quad (7)$$

where g_1 and g_2 are the statistical weights of the lower and upper state, respectively. Tabulated values of cross sections $\sigma_{21} \equiv \sigma_{21}(v_0)$ are computed at the line center v_0 .

Substituting Eqs. (1) and (2) into Eq. (3), we obtain

$$\begin{aligned} \Phi &= \frac{A}{4\pi z^2} NA_{21} \int_0^\infty x(v) \varphi(v) dv \\ &\simeq \frac{A}{4\pi z^2} NA_{21} x(v_0) \varphi(v_0) \Delta v, \end{aligned} \quad (8)$$

where Δv is the laser line width. The second equality follows because the line width for a CW laser, and therefore the frequency range over which x is nonzero, is typically much smaller than the Doppler width. From this we see that the atomic quantity that best characterizes the LGS return flux, is

$$\varepsilon = NA_{21} x(v_0). \quad (9)$$

We shall call ε the *return flux coefficient* for the transition. It has units of photons $\text{s}^{-1} \text{m}^{-2}$.

Also of interest is the dimensionless product $N\sigma_{21}$, which determines the maximum possible optical depth. Specifically, τ is bounded by $-N\sigma_{21} \leq \tau \leq N\sigma_{12}$ [10]. Therefore, ASE is not possible if $N\sigma_{21} < 1$.

Several other physical processes also play a role in the response of atoms to laser excitation. Atomic collisions effectively reset atoms that have been excited, either returning them to the ground state, or causing a transition to a different excited state. The latter process makes the atom unavailable for excitation by the laser. At the same time, collisions impart a velocity to the atom, generally pushing it out of the velocity interval that can be excited by the laser (the “velocity class”). In equilibrium this is balanced by collisions that move atoms into the velocity class. Those atoms are in the ground state as the collision energies, typically ~ 0.02 eV, are not sufficient to excite the atom from the ground state. Therefore any individual atom is effectively “reset” to the ground state on a time scale equal to the mean time between collisions.

Collision rates vary by species and altitude. Rates for the species of interest are calculated in Appendix A, for a range of altitudes.

In order to be useful for AO, a transition should have a high spontaneous transition rate to the lower state (Einstein A coefficient). Also, as most atoms will be in the ground state, there should be a path to the upper state from the ground state, with a high transition probability (Einstein B coefficient). As the Einstein coefficients are related, it is sufficient to consider transitions that have a large A coefficient.

A second consideration is that the upper state should not have many transitions to metastable states, which have low A coefficients. In such a situation, atoms can become trapped in those states, reducing the number of atoms available for the desired transition. Ultimately, atoms trapped in metastable states will be reset at the collision rate.

The performance of PLGS will critically depend on the wavelengths and return flux of the available transitions. For amplitude θ of a Zernike mode (except for piston), the ratio of the difference in amplitude $\Delta\theta$ at different wavelengths, is related to the ratio of refracting indexes by [15]

$$p \equiv \frac{\theta}{\Delta\theta} = \frac{n_{\lambda_{\text{obs}}} - 1}{n_{\lambda_1} - n_{\lambda_2}}, \quad (10)$$

where n_{λ_1} and n_{λ_2} are the refractive indexes at wavelengths of the measurement and $n_{\lambda_{\text{obs}}}$ is the refractive index of the wavelength at which the amplitude of the Zernike mode is determined. The dimensionless ratio p is called the *penalty factor*. Smaller values of p correspond to greater PLGS performance. We take $\lambda_{\text{obs}} = 500$ nm as the reference wavelength.

The impact of return flux and penalty factor can be captured in a single merit function. The signal-to-noise ratio for the measurement of the atmospheric wavefront tilt is proportional to the square root of the return flux and inversely proportional to the penalty factor [15]. Therefore, $\varepsilon^{1/2}/p$ is a measure of relative PLGS performance. To make this dimensionless, we divide by the same quantity evaluated for a reference system. We thus define the PLGS merit function

$$q \equiv \frac{p_0}{p} \left(\frac{\varepsilon}{\varepsilon_0} \right)^{1/2}, \quad (11)$$

where ε_0 and p_0 are reference values. For these we use the 330.298/2208.370 nm transitions in Na I, which is the highest-performance system employing single-photon excitation. In all cases, the return flux coefficient used is that of the weaker line.

When discussing atomic transitions we use spectroscopic notation and refer to Fe as Fe I, Fe^+ as Fe II, etc. We refer to transitions having wavelengths greater than 300 nm as “visible” transitions. Shorter-wavelengths are greatly attenuated by the atmosphere so we refer to those as “vacuum-ultraviolet” transitions. We refer to transitions having an Einstein A coefficient greater than 10^6 s^{-1} as “strong transitions”, and “weak transitions” otherwise. This distinction is somewhat arbitrary but serves to generally separate permitted lines from forbidden lines. An excitation scheme that uses two different transitions to reach an excited state will be called a “two-step” process. One that uses two photons to excite a single transition, using a virtual intermediate state, will be called a “two-photon” process.

Transition wavelengths described in the text and listed in the tables in the following sections are in air for wavelengths greater than 185 nm and in vacuum otherwise.

3. ANALYSIS AND RESULTS

The data set employed for this analysis is the atomic database of the National Institute of Standards and Technology (NIST) [28]. Complete data for all transitions were downloaded and a computer program was written to apply various criteria to identify transitions of interest for AO. We examined all excited states that could be reached from the ground state by at most two successive excitations using wavelengths greater than 300 nm. For species in which no such transitions are possible, two-photon excitation was considered. For every such state, all possible downward transitions were examined, and the excitation fraction x of the excited state was computed according to the methods presented in Appendix B. A specific energy density of $\rho_v = 10^{-12} \text{ J m}^{-3} \text{ Hz}^{-1}$ was assumed for the laser excitation. This is at the high end of range of energy densities that can be achieved with current AO lasers. A complete listing of all such transitions that have $A \geq 10^7 \text{ s}^{-1}$ is available from the authors upon request. From this and the data of Table 1, the return flux coefficient was computed. For PLGS, the penalty factor p and merit function q were computed for all downward transitions.

Our results are shown in Tables 2–9. Table 2 lists all transitions, for all species, that have a return flux coefficient $\varepsilon > 10^{18}$ photons $\text{s}^{-1} \text{m}^{-2}$. In this, and subsequent tables, λ_{ex} refers to the excitation wavelength(s) employed to reach the excited state,

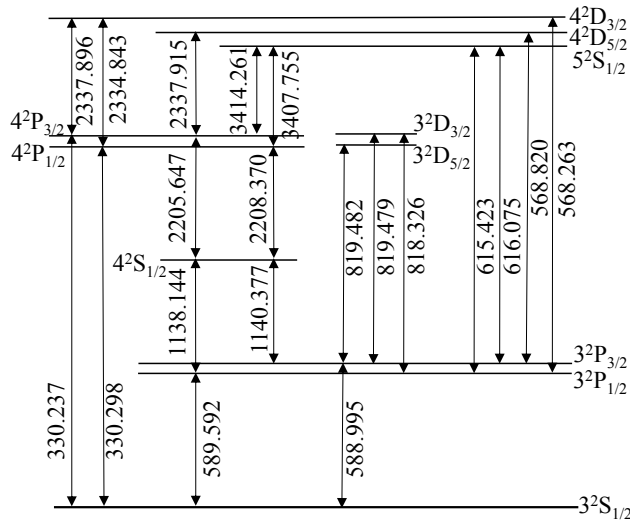


Fig. 1. Low-lying energy levels of the sodium atom and transitions of interest.

and λ is the wavelength of the downward transition. Unless otherwise specified, values of p are computed with respect to the smallest wavelength.

We now discuss individual atomic species in more detail.

A. Sodium

Sodium is most-often employed for the generation of LGS. Neutral sodium is used as it is more abundant than ionized forms. Averaged over all seasons and latitudes, the observed ratio of Na^+ to Na is between 0.2 and 0.25 [29]. An energy level diagram of neutral sodium, indicating the lifetimes and wavelengths for selected transitions is shown in Fig. 1. For simplicity, fine-structure splitting of the levels is not shown.

At visible wavelengths, Na I has four strong transitions from the ground state, at 330.237, 330.298, 588.995 and 589.592 nm. The latter two form the sodium D doublet. A fifth transition, at 388.390 nm, has a very-small rate ($A = 6.95 \times 10^{-4} \text{ s}^{-1}$).

The transition between the $3S_{1/2}$ ground state and the $3P_{3/2}$ excited state, the D_2 line, has been of interest for adaptive optics since 1985 [2]. Laser-induced excitation followed by spontaneous emission produces the backscattered photons of the LGS. The LGS return flux is limited by the low abundance and small absorption cross section, $N\sigma_{12} \simeq 3\%$. In practice, the D_{2b} line, which involves only transitions between the $F = 2$ lower and $F = 1, 2$ and 3 upper sub-levels, is used for AO. A CW laser can excite 3/4 of the available atoms to the upper state, corresponding to the ratio 15/20 of the number of magnetic substates in the upper levels to the total. Current AO lasers are sufficiently powerful that the excitation fraction closely approaches this limit. However, only a fraction of the total number of sodium atoms are available for excitation because of limited spectral overlap as the laser linewidth is typically much smaller than the sodium linewidth. This limitation might be overcome with further development of efficient broad-band modeless pulsed lasers [30].

Table 2. Transitions for a monochromatic LGS having $\lambda \geq 300 \text{ nm}$, $\lambda_{\text{ex}} \geq 150 \text{ nm}$ and $\log(\epsilon) > 18.3$.

Species	λ_{ex} (nm)	λ (nm)	$\log(\epsilon)$	$\log(N\sigma_{21})$
Na I	588.995	588.995	21.20	-1.50
	589.592	589.592	21.07	-1.50
	330.237	2205.647	20.00	-0.75
	330.237	588.995	19.83	-1.50
	330.298	2208.370	19.82	-0.75
	330.237	1140.377	19.82	-1.19
	330.298	588.995	19.65	-1.50
	330.298	1140.377	19.65	-1.19
	330.237	330.237	19.61	-3.61
	330.237	589.592	19.52	-1.50
	330.237	1138.144	19.52	-1.49
	330.298	330.298	19.44	-3.61
	330.298	589.592	19.37	-1.50
	330.298	1138.144	19.35	-1.49
	285.281	5426.880	19.20	-0.25
	285.281	588.995	19.18	-1.50
	285.301	5434.170	18.98	-0.25
	285.301	588.995	18.95	-1.50
	285.281	1140.377	18.93	-1.19
	285.281	1074.645	18.91	-2.65
	285.281	589.592	18.87	-1.50
	285.281	616.075	18.78	-2.54
	268.034	588.995	18.71	-1.50
	285.301	1140.377	18.71	-1.19
	285.301	1074.930	18.68	-2.65
	285.301	589.592	18.67	-1.50
	285.281	3414.261	18.64	-0.45
	285.281	1138.144	18.63	-1.49
	268.034	10807.960	18.61	0.14
	285.301	616.075	18.56	-2.54
	285.281	2205.647	18.51	-0.75
	285.281	615.423	18.49	-2.84
	268.043	588.995	18.45	-1.50
	285.301	3414.261	18.42	-0.45
268.034	1140.377	18.41	-1.19	
285.301	1138.144	18.41	-1.49	
268.034	589.592	18.40	-1.50	
268.043	10823.050	18.36	0.14	
259.387	588.995	18.34	-1.50	
285.281	3407.755	18.34	-0.75	
330.237	9090.560	18.33	-0.57	
330.237	819.482	18.33	-1.15	
268.034	2440.182	18.32	-2.08	
268.034	864.993	18.31	-3.44	
Fe I	371.993	371.993	20.40	-2.08
	385.991	385.991	18.72	-2.26
	344.061	344.061	18.49	-2.16
	367.991	373.713	18.18	-2.14
	296.690	373.486	18.17	-1.33
	216.677	349.710	18.13	-2.42
	302.064	302.064	18.13	-1.68
	261.871	381.584	18.08	-1.21
	302.064	382.042	18.07	-1.43
	344.061	349.057	18.05	-2.59

Table 2. continued

	213.202	340.746	18.04	-1.62
	437.593	646.271	18.04	-3.59
	319.166	516.749	18.03	-2.43
Ca I	422.673	422.673	19.72	-3.34
K I	766.490	766.490	19.05	-3.21
	769.896	769.896	18.92	-3.21
Mg I	202.582	1710.866	18.15	-1.55
	202.582	1182.819	18.15	-1.63

Quantitative results for single-photon excitation in Na I are shown in Table 2. In Table 3 we list all transitions in Na I that are available with two-step excitation and have a return flux coefficient $\epsilon > 10^{20}$ photons $\text{s}^{-1} \text{m}^{-2}$. There are many, but even the strongest is two times weaker than the sodium D₂ line.

Of particular interest for PLGS are transitions from the 4P_{3/2} state [16]. This state may be populated directly from the ground state by absorption of a 330 nm photon. De-excitation occurs through two pathways. Approximately 29% decay directly to the ground state, emitting a 330 nm photon and 70% decay to the 4S_{1/2} state, emitting a 2206 nm photon. That state can decay to the ground state via two pathways. About 67% decay via the 3P_{3/2} state, emitting 1140 and 589 nm photons. The remaining decay via the 3P_{1/2} state emitting 1138 and 590 nm photons. About 1.5% of the atoms in the 4P_{3/2} state return to the ground state via the 3D_{5/2} state, emitting 9093, 819 and 589 nm photons.

Table 3. Na I transitions for a monochromatic LGS employing two-step excitation having $\lambda \geq 300$ nm and $\log(\epsilon) > 20$.

λ (nm)	λ_{ex} (nm)	$\log(\epsilon)$	$\log(N\sigma_{21})$
819.482	588.995+819.482	21.00	-1.15
818.326	589.592+818.326	20.89	-1.23
818.326	588.995+819.479	20.68	-1.23
589.592	588.995+819.479	20.68	-1.50
1140.377	589.592+1138.144	20.31	-1.19
588.995	589.592+1138.144	20.31	-1.50
1140.377	588.995+1140.377	20.22	-1.19
568.820	588.995+568.820	20.19	-2.26
819.479	589.592+818.326	20.19	-1.93
588.995	589.592+818.326	20.19	-1.50
588.995	330.237+2337.915	20.18	-1.50
568.263	589.592+568.263	20.10	-2.34
568.820	330.237+2337.915	20.08	-2.26
1138.144	589.592+1138.144	20.01	-1.49

It is also possible to use a 330 nm photon to excite directly to the 4P_{1/2} state, rather than the 4P_{3/2} state, with a comparable transition rate. That state decays directly to the ground state with a 29% probability, to the 4S_{1/2} state with a 70% probability, and to the 3D_{3/2} state with a 1.6% probability, producing a 9140 nm photon. The 3D_{3/2} state decays to ground state via the 3P_{1/2} state, producing 818 and 590 nm photons, or via the 3P_{3/2} state, producing 819 and 589 nm photons.

We searched for all possible PLGS line combinations employing single-photon excitation in Na I, with the condition that they have a return flux greater than 10^{17} photons $\text{s}^{-1} \text{m}^{-2}$ (four orders of magnitude weaker than the Na D₂ lines) and a penalty factor less than 50. The results are shown in Table 4. The only possibilities are the two already mentioned.

Table 4. Na I transitions for a PLGS. All transitions having $q > 0.4$ and $\lambda_{\text{ex}} \geq 300$ nm are listed.

λ_{ex} (nm)	q	p	λ_1 (nm)	$\log(\epsilon_1)$	λ_2 (nm)	$\log(\epsilon_2)$
330.237	1.00	18.59	330.237	19.61	2205.647	20.00
	0.94	19.74	330.237	19.61	1140.377	19.82
	0.84	19.74	330.237	19.61	1138.144	19.52
	0.72	25.86	330.237	19.61	588.995	19.83
	0.65	25.84	330.237	19.61	589.592	19.52
330.298	0.82	18.60	330.298	19.44	2208.370	19.82
	0.77	19.75	330.298	19.44	1140.377	19.65
	0.69	19.75	330.298	19.44	1138.144	19.35
	0.59	25.87	330.298	19.44	588.995	19.65
	0.54	25.85	330.298	19.44	589.592	19.37

Several transitions involving two-step excitation have been discussed in the literature. The processes of 3S_{1/2} → 3P_{3/2} → 4D_{5/2} (589 + 569 nm) [15], 3S_{1/2} → 3P_{3/2} → 4S_{1/2} (589 + 1140 nm) [31] and 3S_{1/2} → 3P_{3/2} → 3D_{5/2} (589 + 819.7 nm) [32]. Excitation via the 3P_{1/2} state is also possible but with somewhat lower transition rates.

Atoms excited to the 3P levels can be further excited to the 4D, 4S or 3D levels by absorption of visible or infrared light, provided that this is done within a few ns. Sodium can also be excited from the ground state to the 4D_{5/2} level by absorption of two 578 nm photons. This is a non-linear process involving a virtual intermediate state, requiring picosecond pulses and a laser irradiance on the order of 10^{10} W m^{-2} [31].

All possible combinations employing two-step excitation in Na I are listed in Table 5. The selection criteria is $q > 0.4$. The strongest of these is 589 + 569 nm excitation producing lines at 569 and 2334 nm. These transitions would provide a SNR that is 0.79 times the single-photon excitation transitions shown in Table 4. That is roughly equivalent to a decrease to 65% in LGS return flux.

Table 5. Na I transitions for a PLGS employing two-step excitation. All transitions that have $q > 0.4$ and $\lambda_{\text{ex}} \geq 300$ nm are listed. The last line for each excitation scheme shows the return flux coefficient for the first excitation wavelength.

λ_{ex} (nm)	q	p	λ_1 (nm)	$\log(\epsilon_1)$	λ_2 (nm)	$\log(\epsilon_2)$
588.995	0.79	18.55	330.237	19.41	2337.915	19.95
+ 568.820	0.79	18.59	330.237	19.41	2205.647	19.79
	0.75	19.74	330.237	19.41	1140.377	19.62
	0.67	19.74	330.237	19.41	1138.144	19.32
	0.55	26.69	330.237	19.41	568.820	20.19
	0.51	25.84	330.237	19.41	589.592	19.32
	0.45	60.81	568.820	20.19	2337.915	19.95
			588.995	20.78		
589.592	0.71	18.56	330.298	19.32	2334.843	19.86
+ 568.263	0.71	18.60	330.298	19.32	2208.370	19.70
	0.67	19.75	330.298	19.32	1140.377	19.60
	0.66	19.75	330.298	19.32	1138.144	19.30
	0.59	18.56	330.298	19.32	2337.896	19.16
	0.51	25.87	330.298	19.32	588.995	19.82

Table 5 continued

	0.49	18.60	330.298	19.32	2205.647	19.00
	0.49	26.71	330.298	19.32	568.819	19.40
	0.49	26.73	330.298	19.32	568.263	20.10
	0.41	60.69	568.263	20.10	2334.843	19.86
			589.592	20.65		
588.995	0.57	18.56	330.298	19.13	2334.843	19.67
+ 568.819	0.57	18.60	330.298	19.13	2208.370	19.51
	0.54	19.75	330.298	19.13	1140.377	19.41
	0.53	19.75	330.298	19.13	1138.144	19.11
	0.48	18.56	330.298	19.13	2337.896	18.97
	0.41	25.85	330.298	19.13	589.592	19.98
	0.40	18.60	330.298	19.13	2205.647	18.81
	0.40	26.71	330.298	19.13	568.819	19.21
	0.40	26.73	330.298	19.13	568.263	19.91
			588.995	20.96		
330.237	0.51	18.56	330.298	19.03	2334.843	19.57
+ 2337.896	0.51	18.60	330.298	19.03	2208.370	19.41
	0.51	18.60	330.298	19.03	2205.647	19.64
	0.48	19.75	330.298	19.03	1140.377	19.66
	0.48	19.75	330.298	19.03	1138.144	19.36
	0.43	18.56	330.298	19.03	2337.896	18.87
			330.237	19.25		
588.995	0.50	126.58	589.592	20.68	818.326	20.68
+ 819.479	0.23	126.21	589.592	20.68	819.479	19.99
			588.995	20.91		
589.592	0.50	83.39	588.995	20.31	1140.377	20.31
+ 1138.144	0.35	83.50	588.995	20.31	1138.144	20.01
			589.592	20.87		
588.995	0.49	18.27	330.237	18.99	5426.880	19.01
+ 498.281	0.49	18.28	330.237	18.99	5013.920	19.30
	0.49	18.59	330.237	18.99	2205.647	19.37
	0.47	19.09	330.237	18.99	1477.974	19.49
	0.46	19.74	330.237	18.99	1140.377	19.30
	0.46	19.74	330.237	18.99	1138.144	18.99
			588.995	20.78		
589.592	0.47	18.37	330.237	18.94	3414.261	19.49
+ 615.423	0.47	18.37	330.237	18.94	3407.755	19.19
	0.46	18.59	330.237	18.94	2208.370	19.03
	0.46	18.59	330.237	18.94	2205.647	19.33
	0.44	19.74	330.237	18.94	1140.377	19.33
	0.44	19.74	330.237	18.94	1138.144	19.03
			589.592	20.86		
588.995	0.44	18.37	330.237	18.88	3414.261	19.42
+ 616.075	0.44	18.37	330.237	18.88	3407.755	19.12
	0.43	18.59	330.237	18.88	2208.370	18.96
	0.43	18.59	330.237	18.88	2205.647	19.26
	0.41	19.74	330.237	18.88	1140.377	19.26
	0.40	19.74	330.237	18.88	1138.144	18.96
			588.995	21.03		
589.592	0.44	18.28	330.298	18.88	5434.170	18.92
+ 497.854	0.44	18.29	330.298	18.88	5007.670	19.21
	0.43	18.60	330.298	18.88	2208.370	19.26
	0.42	19.10	330.298	18.88	1476.749	19.40
	0.40	19.75	330.298	18.88	1140.377	19.28
	0.40	19.75	330.298	18.88	1138.144	18.98

Table 5 continued

					589.592	20.66
	330.237	0.40	60.81	568.820	20.08	2337.915
	+ 2337.915			330.237	19.26	19.85

B. Iron

The average iron abundances near the density peak at 90 km is two orders of magnitude higher than that of most other mesospheric metals, and twice that of sodium. Although its cross section is small, the key product $N\sigma_{21}$ is still larger than that of all other metallic elements except sodium. The abundance ratio Fe^+ / Fe is approximately 0.2 above 90 km [33].

Atomic iron has the largest number of spectral lines of all mesospheric species. The iron-group elements have complex transitions with thousands of lines from the vacuum ultraviolet to the infrared. An energy-level diagram for Fe I is shown in Fig. 2. The ground state is split into three fine-structure levels. Only the lowest-energy a^5D_4 state is populated in thermal equilibrium in the mesosphere. There are five strong visible-wavelength transitions from this ground state, at 344.061, 367.991, 371.993, 382.444 and 385.991 nm. Most of these can decay to the other two ground states. The z^5D_3 state, reached by the 372 nm transition from the ground state, has a moderately-strong ($A = 1.15 \times 10^6 s^{-1}$) downward transition to the metastable a^5F_4 state.

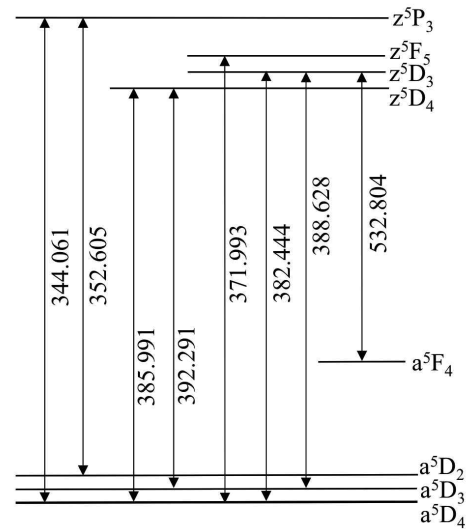


Fig. 2. Selected states and transitions of Fe I.

The strongest transition in Fe I using single-photon excitation has a return flux coefficient of $2.51 \times 10^{20} \text{ photons s}^{-1} \text{ m}^{-2}$ (Table 2). This is six times weaker than the sodium D_2 line. Two-step excitation (Table 6) provides more possibilities, but these are all weaker by at least an order of magnitude.

Fe I has combinations of transitions which have promising wavelengths and penalty factors for PLGS. However, for one-step and two-step excitation, q does not exceed $q > 0.18$ for any combination of wavelengths (Tables 7 and 8).

Fe II has no transitions from the ground state for wavelengths greater than 260 nm. This rules out excitation by ground-based lasers unless two-photon excitation is used. That would require pulsed lasers with very high irradiance.

Table 6. Fe I transitions for a monochromatic LGS employing two-step excitation. All transitions that have $\log(\epsilon) > 19$ and $\lambda_{\text{ex}} \geq 300$ nm are listed.

λ (nm)	λ_{ex} (nm)	$\log(\epsilon)$	$\log(N\sigma_{21})$
355.492	437.593+355.492	19.32	-1.21
314.399	385.991+314.399	19.31	-1.73
381.764	371.993+381.764	19.29	-2.37
380.198	371.993+380.198	19.08	-2.70

Table 7. Fe I transitions for a PLGS employing one-step excitation. All transitions that have $q > 0.1$ and $\lambda_{\text{ex}} \geq 300$ nm are listed.

λ_{ex} (nm)	q	p	λ_1 (nm)	$\log(\epsilon_1)$	λ_2 (nm)	$\log(\epsilon_2)$
319.323	0.10	26.39	319.323	17.90	517.160	17.90

C. Magnesium

Magnesium is one of the more abundant meteoritic constituents, 9.6% by mass, so that meteoric ablation should inject large quantities of this metal into the MLT region [22]. Compared to other meteoric metals, magnesium has the largest ionization fraction, with a ratio Mg^+/Mg in the range 4 to 12 [22].

Mg I has six strong transitions from the ground state, all in the vacuum ultraviolet. The strongest of these goes to the 3^1P_1 state, with a wavelength of 285.213 nm and a rate ($A_{21} = 4.91 \times 10^8 \text{ s}^{-1}$) that is an order of magnitude greater than that of the sodium D lines. The only other downward transitions from this upper state are forbidden lines that have negligible rates. In vacuum, this would be a strong candidate for LGS, however, the wavelength is beyond the atmospheric cutoff.

Table 8. Fe I transitions for a PLGS employing two-step excitation. All transitions that have a de-excitation $q > 0.1$ and $\lambda_{\text{ex}} \geq 300$ nm are listed. In brackets in the last line for each excitation scheme the return flux coefficient for the first excitation wavelength is shown.

λ_{ex} (nm)	q	p	λ_1 (nm)	$\log(\epsilon_1)$	λ_2 (nm)	$\log(\epsilon_2)$
437.593	0.12	25.41	361.207	18.17	973.857	18.01
+ 361.207	0.11	27.33	371.993	18.85	973.857	18.01
			437.593	16.06		
385.991	0.12	40.78	371.993	18.49	561.564	18.49
+ 532.418	0.10	44.57	371.993	18.49	532.418	18.38
			385.991	18.18		

Mg II has two transitions from the ground state that have rates greater than 10^8 s^{-1} . These go to the $3^2P_{1/2}$ and $3^2P_{3/2}$ states, with wavelengths of 280.271 and 279.553 nm respectively. Both of these upper states return directly to the ground state, with no other significant transitions. Given the high abundance of Mg^+ (twice that of Na), these would be very good candidates for LGS, but they are beyond the atmospheric cutoff.

Mg II does have strong emission lines in the visible region [34] (Fig.3). However, populating these levels from the ground state requires photons having wavelengths of 124 nm or less. This probably rules out Mg^+ for ground-based adaptive optics.

D. Silicon

Silicon is one of the most abundant elements in cosmic dust, comprising around 11% by mass, and meteoric ablation injects

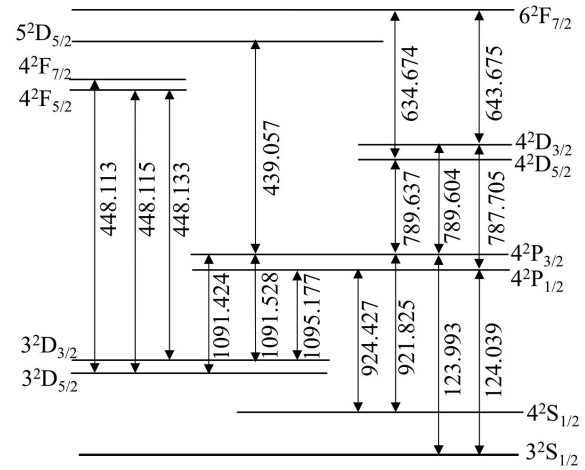


Fig. 3. Selected states and transitions of Mg II.

a significant amount of Si into the atmosphere [24]. However, neutral Si is oxidized to SiO very rapidly by reaction with O_2 at the altitude of maximum ablation, around 90 km. Si^+ , SiO, and $\text{Si}(\text{OH})_4$ are predicted to be the major silicon species above 80 km. Below 97 km the dominant sink is $\text{Si}(\text{OH})_4$. The column density of Si^+ varies seasonally by an order of magnitude and peaks at $4.0 \times 10^9 \text{ cm}^{-2}$ during the summer [24].

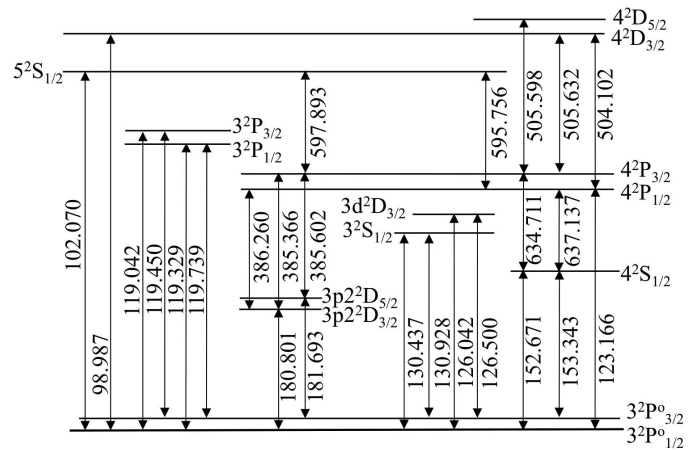


Fig. 4. Selected states and transitions of Si II.

Singly-ionized Silicon has several strong visible-light transitions, as shown in Fig. 4 [35]. However, excitation from the ground state requires UV photons. The ground state is a doublet ($3^2P_{1/2}$, $3^2P_{3/2}$), separated by 0.0356 eV. This is comparable to the mean particle energy of $3kT/2 \approx 0.023$ eV, so both states will be populated. Transitions can occur from the lower ground state to the $4P_{1/2}$ state, followed by a 637 nm visible-light transition, but this requires a 123-nm photon. The lowest-energy transitions from either ground state to the 4P levels requires a 123-nm photon. There is a transition from the ground state to the $3^2P_{3/2}$ state, but this is quite weak ($A_{21} = 2.54 \times 10^6 \text{ s}^{-1}$). This likely rules out SI II as a viable candidate for AO, and indeed no transitions met our thresholds for inclusion.

E. Calcium

Lidar measurements of calcium showed a peak density of 2×10^7 atoms m^{-3} , about 200 times lower than the typical sodium atom density and 400 times lower than that of iron [36]. The annual average Ca^+/Ca column density ratio is 2.4, the second largest ratio after magnesium. In comparison, the ratios of Na^+/Na and Fe^+/Fe are only about 0.2 [37]. Ca^+ is the dominant form above 90 km altitude, peaking near 105 km.

Ca I has a strong transition from the ground state to the 3^1P_1 state with a rate of $2.18 \times 10^8 \text{ s}^{-1}$ and a wavelength of 422.673 nm. The upper state returns directly to the ground state, with no other transitions. The only problem here is the low abundance. As can be seen in Table 2, the return flux coefficient is about 30 times smaller than that of the sodium D_2 line.

Table 9. Ca I transitions for a monochromatic LGS employing two-step excitation having wavelength $\lambda \geq 300$ nm and return-flux coefficient $\log(\epsilon) > 19$.

λ (nm)	λ_{ex} (nm)	$\log(\epsilon)$	$\log(N\sigma_{21})$
585.745	422.673+585.745	19.07	-3.43
430.774	657.278+430.774	19.01	-3.35

Fig. 5 shows the relevant energy levels and transitions of Ca^+ [38]. Excitation from the ground state to the $4P_{1/2}$ and $4P_{3/2}$ levels is possible using 397 nm and 393 nm photons, respectively. These states decay quickly to the ground state and also, with 7% probability, to the $3D_{3/2}$ and $3D_{5/2}$ states, emitting 866 nm, 850 nm and 854 nm photons. These states are metastable, so most of the atoms excited from the ground state using a UV laser will become trapped in these states. No lines of Ca II met the criteria for inclusion in Table 2.

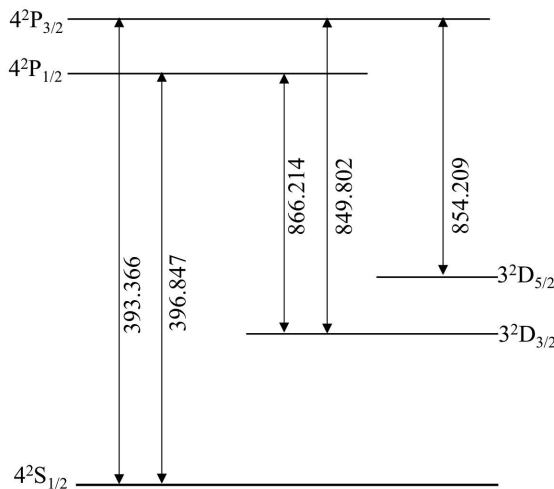


Fig. 5. Selected states and transitions of Ca II.

F. Potassium

Potassium has relatively low abundance in the upper atmosphere, having a column density that is about two orders of magnitude less than that of Na. For neutral potassium atoms, many transitions covering the visible light range have high transition probabilities. The relevant energy levels and transitions are shown as Fig. 6. Its persistent lines are 769.896, 766.490, 404.414

and 404.721 nm. Other strong lines having slightly smaller transition probabilities occur at higher energy levels. Direct transitions to and from the ground state are possible at 766.490 and 769.896 nm. These have cross sections that are comparable to that of the sodium D_2 line. However, the relatively low column density of potassium results in return flux coefficients that are two orders of magnitude smaller.

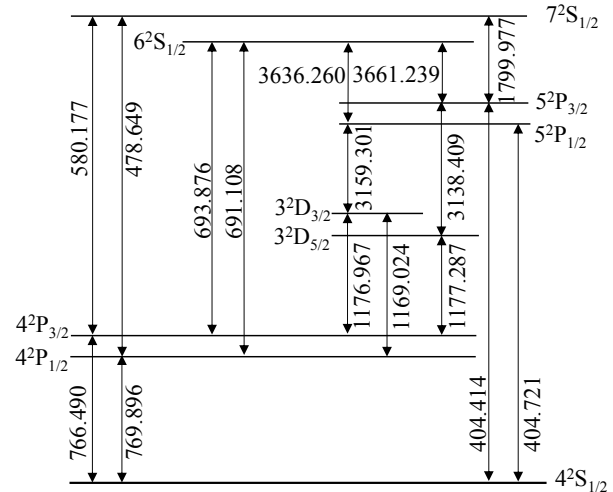


Fig. 6. Selected states and transitions of K I.

Potassium can also be excited directly from the ground state to the $5P_{1/2}$ and $5P_{3/2}$ levels. These have a path back to the ground state via the 3D states and 4P states, producing strong lines at 3139.265, 3160.163, 1169.024 and 1176.967 nm, in addition to the 766.490 and 769.896 nm doublet. This would be an attractive system for PLGS if it was not for the relatively low abundance.

G. Nitrogen

In the mesosphere, nitrogen molecules are ionized and dissociated by energetic electrons and protons, producing N_2^+ by direct ionization and N^+ by dissociative ionization. Secondary electrons associated with ionization produce N in both the ground and 2D states. At 80 km atomic nitrogen has a peak density of $2 \times 10^8 \text{ cm}^{-3}$, falling to 10^6 cm^{-3} at 70 km [25]. The estimated column density of atomic nitrogen is $\sim 1 \times 10^{14} \text{ cm}^{-2}$.

The most relevant energy levels and transitions of atomic NI and singly-ionized NII are shown in Fig. 7. It can be seen that NII has many more strong emission lines in the visible range than does NI. Furthermore, nitrogen-discharge experiments [39] show that the optical emission spectrum in the visible and UV regions, is quite complex with multiple-peaks and many blended lines.

Direct transitions from the ground state require vacuum-ultraviolet photons, even using two-photon excitation. This likely rules out nitrogen for ground-based AO systems.

H. Oxygen

Atomic oxygen (O) is a fundamental component in chemical aeronomy of Earth's MLT region extending from approximately 50 km to over 100 km altitude. Primarily, O is generated through photolysis of molecular oxygen by UV radiation. The peak atomic oxygen concentrations, $\sim 6.0 - 6.5 \times 10^{17} \text{ m}^{-3}$, are found at an altitude of approximately 95 km [26]. Assuming an atomic

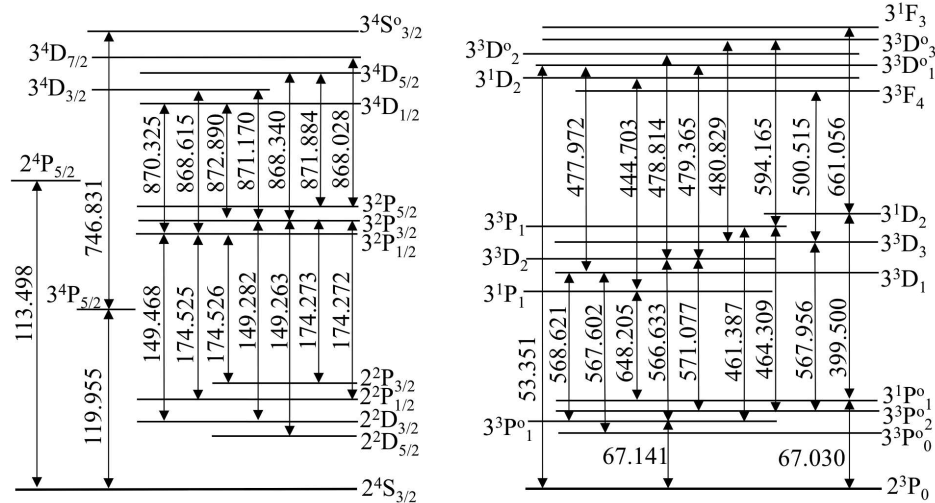


Fig. 7. Energy level diagram of N I (left) and N II (right).

oxygen column width of 10 km in the mesosphere, the estimated column density of atomic oxygen is $\sim 6.0 - 6.5 \times 10^{21} \text{m}^{-2}$.

Energy level diagrams for O and O^+ are shown in Fig. 8. The triplet at ~ 130 nm has been observed in the cometary spectra from above the Earth's atmosphere [40]. These lines arise when O atoms in the ground state are excited to the $5S_1$ state by solar photons. In the visible spectrum region, several astrophysically-important forbidden transitions exist. For O, these are the red doublet at 630.030 nm and 636.377 nm, arising from transitions between the $2D_2$ and the $2P_2$ and the $2P_1$ levels respectively, and the green line at 557.734 nm from the $2D_2$ and $2S_0$ levels. These are magnetic dipole and electric quadrupole transitions respectively. These forbidden oxygen emission lines likely arise from atoms produced directly in the excited $2S_0$ or $2D_2$ states by photo-dissociation of parent molecules such as H_2O , CO and CO_2 . In O^+ , the doublet at 372.602 and 372.882 nm arises from transitions from the $2D_{3/2}$ and $2D_{5/2}$ levels to the $2S_{3/2}$ ground state. As with nitrogen, $N\sigma_{21}$ is high for permitted transitions in oxygen, but low for the forbidden transitions.

In O, strong visible lines arise from transitions between the $3P$ and $3S$ levels, and also the $5S_1$ level. Visible lines can also occur from states above the $5S_1$ energy level. Each line is a doublet or triplet due to hyperfine structure. However, all these lines require vacuum-ultraviolet photons for excitation from the ground state.

In O^+ , strong visible lines result from transitions from the $3P$ and $3D$ levels to the $3P$ levels, and also the $3S_{1/2}$ and $3P_{3/2}$ levels. In this case there are no direct transitions from the ground state to the upper states involved, and transitions to the lower states require photons of wavelength 54 nm or less.

I. Hydrogen

Atomic hydrogen (H) is also a fundamental component in the photochemistry and energy balance of the mesopause region between approximately 80 and 100 km altitude. H is generated primarily by photolysis of water vapor and participates in a highly-exothermic reaction with ozone. During the day, atomic hydrogen concentrations peak in excess of $2.25 \times 10^{14} \text{m}^{-3}$ at higher latitudes near 85 km [27]. The estimated column density of atomic hydrogen is $\sim 2 \times 10^{18} \text{m}^{-2}$.

Hydrogen and hydrogen-like ions have familiar Lyman,

Balmer, and Paschen spectral series. Hydrogen emission spectral lines in the visible range include Balmer lines at 410.173, 434.047, 486.134, and 656.283 nm wavelengths, corresponding to transitions to the $n = 2$ level. All energy levels for a given principal quantum number n are degenerate. Transitions from the ground state require vacuum-ultraviolet photons having wavelengths of 122 nm or less.

J. Carbon

Meteoritic ablation injects a significant amount of carbon into the mesosphere. However, atomic carbon is a very short-lived species. It is stabilized in various multi-atomic structures having different molecular configurations. The carbon monoxide (CO) mixing ratio increases steeply with altitude in the mesosphere and in the lower part of the thermosphere is a result of the photolysis of carbon dioxide (CO_2) [41]. Additionally, as the chemical lifetime of CO is much longer than the characteristic dynamical times, this gas is an excellent tracer of dynamics due to its strong $4.7 \mu\text{m}$ transition.

The most common oxidation state of carbon in inorganic compounds is +4, while +2 is found in carbon monoxide. The four outer electrons of carbon are valence electrons, so its ionization energies are much higher than those of most other elements. Short wavelength UV photons are needed to excite the atoms from the ground state, making excitation using a ground-based laser unfeasible. Also, there is little information about the detailed distribution and abundance of carbon and their ions in mesosphere, so carbon and related species are not considered further here.

4. DISCUSSION

It can be seen from Table 2, that the sodium D_2 line provides the highest return flux of all possible transitions, including two-step excitation schemes. This is due to its relatively-large natural abundance and large cross section compared to other metal atoms. Mg^+ and Si^+ have stronger lines, but lack an effective scheme for excitation from the ground state. Although the column density of Fe is twice that of sodium, its lower cross-section results in a return flux that is one to two orders of magnitude smaller.

tion will be to limit the extent of the emitting region along the line of sight.

5. SUMMARY AND CONCLUSIONS

We have reviewed transitions of atoms and ions in the upper atmosphere of interest for AO. Besides Na, which is used extensively by current systems, Fe, Mg, Si, Ca, K all have potential uses. Iron has the highest abundance and the largest number of transitions. However, its return flux is less than that of sodium due to lower cross sections.

Our results confirm the general presumption of the LGS community that Fe is not as well-suited as Na for PLGS. However, we find that one-step excitation at 330 nm may be more suitable than two-step excitation at 569 + 589 nm. Detailed simulations, using Bloch equations and including the effects of Zeeman splitting, would be a useful next step to evaluate the potential of these excitation schemes.

Mg⁺ and Si⁺ have high abundance and several very-strong visible-light transitions. However they require vacuum ultraviolet photons for excitation that appear to be implausible even with two-photon excitation.

Amplified spontaneous emission using metallic species appears to be unfeasible because of the small optical depths. A high abundance is required for ASE, so nitrogen and oxygen are likely the only atoms that could be used.

A. ATOMIC COLLISION RATES IN THE MESOSPHERE AND LOWER THERMOSPHERE

We wish to estimate the collision rates for various metallic atoms and ions in the mesosphere and lower thermosphere (MLT) region. The atmospheric composition in the MLT is essentially the same as in the troposphere, consisting almost entirely of three species, N₂, O₂ and Ar. Their fractions, by volume, are approximately 78%, 21% and 1% respectively. The species of interest to us are Na, Fe, Ca, Si, Mg, K, N, O, H and their ions.

The collision rate R , for a given atom, is given in terms of the collision cross-section Q and the number densities n for the dominant atomic and molecular species. For atom i , interacting with field atoms or molecules j ,

$$R_i = \sum_j n_j Q_{ij} v_{ij}, \quad (\text{A1})$$

where v_{ij} is the relative velocity. For a Maxwell-Boltzmann distribution at temperature T , the RMS relative velocity of an atom or molecule of mass m_i and one of mass m_j is,

$$v_{ij} = \sqrt{v_i^2 + v_j^2} = \sqrt{\frac{8kT}{\pi\mu_{ij}}}, \quad (\text{A2})$$

where $\mu_{ij} = m_i m_j / (m_i + m_j)$ is the reduced mass. The low-energy collision cross section between two atoms is well-approximated by the hard-sphere model,

$$Q_{ij} = \pi(r_i + r_j)^2, \quad (\text{A3})$$

where r_i and r_j are the atomic radii. For a diatomic molecule j , the situation is more complicated. Modelling the molecule by two spheres of radius r_j in contact, the appropriate geometrical cross section is the projected area A of two spheres of radius $r = r_i + r_j$, having centres separated by a distance d . The separation depends on the angle θ between the axis of the molecule and the velocity vector, $d = 2r_j \sin \theta$. To find the mean cross-section

we average over this angle, assuming an isotropic velocity distribution. From plane geometry,

$$A = 2\pi r^2 - 2r^2 \arccos\left(\frac{d}{2r}\right) + \frac{d}{2} \sqrt{4r^2 - d^2}. \quad (\text{A4})$$

The frequency with which a particular angle θ appears is proportional to $\sin \theta$, so

$$\begin{aligned} Q_{ij} &= \frac{4}{\pi} \int_0^{\pi/2} A \sin^2 \theta d\theta, \\ &= 2\pi r^2 + \frac{r^4 + 2r^2 r_j^2 - 3r_j^4}{\pi r_j^2} \operatorname{arcsinh}\left(\frac{r_j}{\sqrt{r^2 - r_j^2}}\right) \\ &\quad - \frac{r^3 - 3r r_j^2}{\pi r_j} + \frac{32r_j r}{3\pi\sqrt{2\pi}} {}_3F_2\left[2, \frac{1}{2}, \frac{1}{2}; \frac{5}{2}, \frac{3}{2}; \left(\frac{r_j}{r}\right)^2\right], \end{aligned} \quad (\text{A5})$$

where ${}_3F_2$ is a generalized hypergeometric function.

Atomic radii are taken from [43]. For the atmospheric density and temperature the MSIS-E-90 atmospheric model was used [21]. These were evaluated, for a latitude of 30° and longitude of 0°, at midnight on the first day of each month, and the average over a full year was computed. The resulting mean cross sections for the atoms and ions of interest, colliding with N₂, O₂ and Ar, are listed in Table A1. The computed collision rates are listed in Tables A2 and A3. For comparison, Holzlöhner et al. [6] estimated a Na – O₂ collision rate of 1/(35 μs) at an altitude of 92 km, which is within a factor of two of our estimate.

Table A1. Mean collision cross sections.

Atom	mass (amu)	radius (nm)	cross section (nm ²)		
			N ₂	O ₂	Ar
Na	22.990	0.191	0.565	0.550	0.277
Fe	55.845	0.127	0.315	0.303	0.171
Mg	24.305	0.162	0.443	0.429	0.226
Si	28.085	0.109	0.257	0.247	0.145
Ca	40.078	0.197	0.593	0.577	0.288
K	39.098	0.237	0.790	0.771	0.370
N	14.007	0.070	0.152	0.144	0.097
O	15.999	0.066	0.143	0.135	0.093
Ar	39.948	0.106	0.248	0.238	0.141
H	1.008	0.070	0.152	0.144	0.097

Table A2. Collision rates, in units of 10² s⁻¹, for metallic species.

altitude (km)	Ca	Fe	K	Mg	Na	Si
75	2449	1219	3283	2062	2675	1150
80	1108	551.7	1486	933.3	1211	520.7
85	484.1	241.0	649.1	407.7	528.8	227.5
90	203.7	101.4	273.1	171.5	222.5	95.70
95	82.66	41.15	110.8	69.60	90.28	38.84
100	32.65	16.26	43.77	27.49	35.65	15.34
105	13.08	6.515	17.54	11.01	14.28	6.147
110	5.662	2.821	7.590	4.766	6.181	2.661
115	2.740	1.365	3.673	2.306	2.991	1.288
120	1.489	0.742	1.996	1.253	1.625	0.700

Table A3. Collision rates, in units of 10^2 s^{-1} , for non-metallic species.

altitude (km)	Ar	H	N	O
75	1023	2592	833.3	748.7
80	463.0	1173	377.1	338.8
85	202.3	512.3	164.7	148.0
90	85.10	215.5	69.30	62.27
95	34.54	87.46	28.13	25.27
100	13.64	34.54	11.11	9.982
105	5.468	13.83	4.451	4.000
110	2.367	5.984	1.926	1.731
115	1.146	2.895	0.932	0.838
120	0.623	1.573	0.507	0.455

B. TRANSITION RATES IN A MULTI-LEVEL ATOM

In a multi-level atom, with states $j, j = 0, 1, \dots, n-1$, the fraction of atoms x_j for which the electron is in state j is determined by n rate equations

$$\dot{x}_j = \Gamma_{jk} x_k. \quad (\text{B1})$$

Here Γ_{jk} specifies the net transition rate between states j and k . These equations are not linearly independent because the occupations fractions are related by the constraint

$$\sum x_k = 1. \quad (\text{B2})$$

This condition can be used to eliminate one of the variables, x_0 say, which results in a set of $n-1$ linearly-independent inhomogeneous equations

$$\dot{x}_j = M_{jk} x_k + b_j, \quad j = 1, 2, \dots, n-1. \quad (\text{B3})$$

The quantities M_{jk} and b_j depend on transition rates and the radiation energy densities at the transition wavelengths. If the radiation energy densities can be regarded as independent of time, these quantities are constant and the equations are readily solved using standard techniques. The general solution is

$$x = \sum c_k a_k e^{\lambda_k t} - M^{-1} b, \quad (\text{B4})$$

where λ_k and c_k are the eigenvalues and eigenvectors of M .

The steady-state solution is found by equating the left hand side of Eqn (B3) to zero,

$$x = -M^{-1} b, \quad (\text{B5})$$

Funding. Yunnan Provincial Department of Education; Natural Sciences and Engineering Research Council of Canada (RGPIN-2019-04369); Chinese Academy of Sciences, CAS President's International Fellowship Initiative (2017VMA0013).

Acknowledgement. We thank Profs. D. Budker and R. Holzlohner for comments on an earlier version of the manuscript. PH thanks the National Astronomical Observatories, Chinese Academy of Sciences for hospitality during a sabbatical visit.

Disclosures. The authors declare no conflict of interests.

Data availability. Data underlying the results presented in this paper are available in Refs. [21] and [28]. Selected data for strong transitions in the atomic species discussed here are available from the authors upon request.

REFERENCES

- J. M. Beckers, *Ann. Rev. Astron. Astrophys.*, **31**, 13 (1993).
- R. Foy and A. Labeyrie, *Astron. Astrophys.* **152**, L29 (1985).
- W. Happer, G. J. MacDonald, C. E. Max and F. J. Dyson, *J. Opt. Soc. Am. A*, **11**, 263 (1994).
- J. M. Telle, *Opt. Soc. Am. Tech. Dig. Ser.* **13**, 100 (1996).
- T. W. Fan, T. H. Zhou, and Y. Feng, *Sci. Rep.* **6**, 19859 (2016).
- a R. Holzlohner, S. M. Rochester, D. B. Calia, D. Budker, J. M. Higbie, and W. Hackenberg, *Astron. Astrophys.* **510**, A20 (2010).
- P. W. Milonni, H. Fearn, J. M. Tell and R. Q. Fugate, *J. Opt. Soc. Am. A* **16**, 11 (1999).
- R. Rampy, D. Gavel, S. M. Rochester and R. Holzlohner, *J. Opt. Soc. Am. B* **32**, 2425 (2015).
- F. P. Bustos, R. Holzlohner, S. Rochester, D. B. Calia, J. Hellemeier and D. Budker, *J. Opt. Soc. Am. B* **37**, 1208 (2020).
- P. Hickson, J. Hellemeier and R. Yang, *Opt. Lett.*, **46**, 1792 (2021).
- F. P. Bustos, A. Akulshin, R. Holzlohner, et al., *Proc. SPIE* **10703**, 107030R-1 (2018).
- F. Rigaut and E. Gendron, *Astron. Astrophys.* **261**, 677 (1992).
- S. Esposito, *Proc. SPIE*. **3353**, 468 (1998).
- R. Ragazzoni, "Laser Guide Star Adaptive Optics for Astronomy," Ed. N. Ageorges and C. Dainty, *NATO ASI Series C*, **551**, 125 (2000).
- R. Foy, A. Migus, F. Biraben, G. Grynberg, P. R. McCullough, and M. Tallon, *Astron. Astrophys. Suppl.* **111**, 569 (1995).
- J. P. Pique, I. C. Moldovan, and V. Fesquet, *J. Opt. Soc. Am. A* **23**, 2817 (2006).
- Pfrommer, T. and Hickson, P., *JOSA A*, **27**, A97 (2010)
- D. S. Davis, P. Hickson, G. Herriot, and C-Y She, *Optics Let.*, **31**, 3369 (2006).
- C. Y. She, S. Chen, Z. Hu, J. Sherman, J. D. Vance, V. Vasoli, M. A. White, J. Yu, and D. A. Krueger, *Geophys. Res. Let.* **27**, 3289 (2000).
- C. S. Gardner, *App. Opt.* **43**, 4941 (2004).
- A. E. Hedin, *J. Geophys. Res.* **96**, 1159 (1991), available online at <https://ccmc.gsfc.nasa.gov/modelweb>
- C. L. Whalley, J. C. Gomez-Martin, T. G. Wright, et al., *Phys. Chem. Chem. Phys.*, **13**, 6352 (2011).
- J. M. C. Plane, Air Force Research Laboratory Report AFRL-AFOSR-UK-TR-2010-0005, 22 pp, (2010).
- J. M. C. Plane, J. C. Gomez-Martin, W. Feng, and D. Janches, *J. Geophys. Res. Atmos.* **121**, 3718 (2016).
- A. C. Aikin and H. J. P. Smith, *Phys. Chem. Earth (C)* **25**, 203 (2000).
- M. G. Mlynczak, L. A. Hunt, J. C. Mast, et al., *J. Geophys. Res. Atmos.* **118**, 5724 (2013).
- M. G. Mlynczak, L. A. Hunt, B. T. Marshall, et al., *J. Geophys. Res. Atmos.* **119**, 3516 (2014).
- A. Kramida, Y. Ralchenko, J. Reader, J. and NIST ASD Team (2020). NIST Atomic Spectra Database (ver. 5.8), [Online]. Available: <https://physics.nist.gov/asd> [2020, November 17]. National Institute of Standards and Technology, Gaithersburg, MD. DOI: <https://doi.org/10.18434/T4W30F>
- D. R. Marsh, D. Janches, W. H. Feng, and J. M. C. Plane, *J. Geophys. Res. Atmos.* **118**, 11442 (2013).
- J-P Pique and S. Farinotti, *JOSA B* **20**, 2093 (2003).
- J. Biegert and J. C. Diels, *Phys. Rev. A* **67**, 043403 (2003).
- C. Xu, C. Guo, H-B. Yu, et al., *Appl. Phys. B* **123**, 94 (2017).
- W. H. Feng, D. R. Marsh, M. P. Chipperfield, et al., *J. Geophys. Res. Atmos.* **118**, 9456 (2013).
- D. E. Kelleher and L. I. Podobedova *J. Phys. Chem. Ref. Data* **37**, 267 (2008).
- D. E. Kelleher and L. I. Podobedova, *J. Phys. Chem. Ref. Data* **37**, 1285 (2008).
- J. M. C. Plane, *Nature Chem.* **3**, 900 (2011).
- E. Kopp, *J. Geophys. Res.* **102**, 9667 (1997).
- C. Maurer, C. Becher, C. Russo, J. Eshner, and R. Blatt, *New J. Phys.* **6**, 94 (2004).
- S. Conti, P. I. Porshnev, A. Fridman, et al., *Exp. Therm. Fluid Sci.* **14**, 79 (2001).
- A. L. Cochran and W. D. Cochran, *Icarus* **154**, 381 (2001).

41. K. U. Grossmann, O. Gusev, and P. Knieling, *J. Atmos. Solar-Terr. Phys.* **68**, 1764 (2006).
42. P. Rairoux, H. Schillinger, S. Niedermeier, et al., *Appl. Phys. B* **71**, 573 (2000).
43. A. N. Cox, "Allen's Astrophysical Quantities," Springer, NY (1999).